

# Structure-specific, mode-resolved phonon coherence and specularity at graphene grain boundaries

Zhun-Yong Ong

*Institute of High Performance Computing, A\*STAR, Singapore 138632, Singapore\**

Georg Schusteritsch and Chris J. Pickard

*Department of Materials Science and Metallurgy, University of Cambridge,*

*27 Charles Babbage Road, Cambridge CB3 0FS, United Kingdom and*

*Advanced Institute for Materials Research, Tohoku University 2-1-1 Katahira, Aoba, Sendai, 980-8577, Japan*

(Dated: March 1, 2022)

In spite of their importance for understanding phonon transport phenomena in thin films and polycrystalline solids, the effects of boundary roughness scattering on phonon specularity and coherence are poorly understood because there is no general method for predicting their dependence on phonon momentum, frequency, branch and boundary morphology. Using the recently formulated atomistic  $S$ -matrix method, we develop a theory of boundary roughness scattering to determine the mode-resolved phonon coherence and specularity parameters from the scattering amplitudes. To illustrate the theory, we apply it to phonon scattering in realistic nonsymmetric graphene grain boundary (GB) models derived from atomic structure predictions. The method is validated by comparing its predictions with frequency-resolved results from lattice dynamics-based calculations. We prove that incoherent scattering is almost perfectly diffusive. We show that phonon scattering at the graphene GB is not diffuse although coherence and specularity are significantly reduced for long-wavelength flexural acoustic phonons. Our approach can be generalized to other atomistic boundary models.

Phonon mean free path (MFP) engineering through boundary roughness scattering is a widely used approach to manipulating phonon transport in low-dimensional materials (e.g. silicon nanowires [1, 2]) for thermoelectric and thermal management applications [3, 4] as well as for investigations into fundamental phonon phenomena such as phonon hydrodynamics [5] in layered crystals [6] and ballistic phonons in graphene [7]. In nanostructures, the reduced thermal conductivity is also attributed to boundary roughness scattering [8, 9]. Nonetheless, in spite of its importance for phonon transport, a rigorous quantitative description of how phonons undergo momentum and phase relaxation from boundary roughness scattering still eludes us [3, 9], posing an obstacle to the systematic use of structural modification to control the phonon MFP, while a direct characterization of the specularity is very difficult with current experimental techniques [10]. Although there have been studies using phonon wavepackets to probe boundary scattering [11–15], their use is limited by the considerable difficulty of deriving mode-resolved reciprocal-space information from real-space data in addition to the substantial computational costs.

A major challenge to understanding this mechanism is our inability to predict accurately for a given boundary model the probability of the incident phonon undergoing specular scattering, characterized by the specularity parameter  $\mathcal{P}$  which plays an important role in many boundary scattering models [2, 16, 17] and should vary with phonon frequency, momentum and polarization/branch. In perfectly specular scattering ( $\mathcal{P} = 1$ ) as shown in Fig. 1(a), the incident bulk phonon is scattered coher-

ently by a smooth boundary into well-defined trajectories while in perfectly diffuse scattering ( $\mathcal{P} = 0$ ) or the so-called Casimir limit as shown in Fig. 1(b), the incoming phonon energy is redistributed uniformly over the entire spectrum of outgoing phonon channels, resulting in maximum momentum loss in the direction parallel to the boundary [9]. Another challenge lies in predicting the effect of boundary roughness on coherent and incoherent scattering, an unresolved issue in phonon transport in superlattices where the role of phonon interference in thermal conductivity is still debated [18–21].

In order to address these challenges, we develop in this paper a theory of boundary roughness scattering, based on the recently formulated atomistic  $S$ -matrix method [22], to determine the *mode-resolved* phonon coherence and specularity parameters for boundary models. Unlike existing approaches [23, 24], our method is fully atomistic, not restricted to long-wavelength modes, and distinguishes coherent and incoherent scattering [25–27] by treating boundary roughness in a statistical manner analogous to the theory of multiple scattering in disordered systems [25, 28–30] and conceptually similar to the approach in Ref. [31]. We apply this theory to phonon scattering at the grain boundary (GB) between armchair- and zigzag-terminated graphene like in Fig. 1(c), using realistic nonsymmetric low-energy GB models derived from *ab initio*-based structure predictions [32]. We validate our method by comparing its predictions with the less precise Zhao-Frend method [33] and analyze how the coherence and specularity parameters vary with phonon frequency, momentum and polarization/branch for the

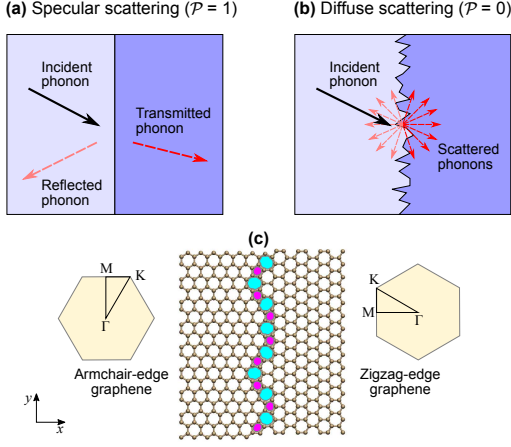


Figure 1. Depiction of (a) perfectly specular versus (b) perfectly diffuse scattering at a boundary, and (c) the graphene GB between armchair- and zigzag-edge graphene. The shape and orientation of their respective Brillouin zones are also shown.

graphene GB.

## I. THEORY AND MODEL

### A. Grain boundary model and $S$ matrix

To treat phonon scattering by the rough (32,32)|(56,0) graphene GB statistically, we need to generate the various possible GB configurations and their interatomic force constant (IFC) matrices. Each (32,32)|(56,0) graphene GB configuration, which consists of an undulating line of pentagon-heptagon defect pairs like in Fig. 1(c), is constructed from an 8-unit random sequence of the two lowest-energy (4,4)|(7,0) graphene GB configurations (GB-II and GB-III in Fig. 2(a)) in Ref. [32], with open-system and periodic boundary conditions in the  $x$  and  $y$  direction, respectively, to yield  $2^8 = 256$  unique GB configurations. Given the large size of the GB models, we use the program GULP [34] and the empirical Tersoff potential [35], with parameters from Ref. [36], to model the C-C interatomic forces instead of more expensive *ab initio* methods and to compute the IFC matrices needed for the atomistic  $S$ -matrix calculations as described in Ref. [22, 37], with details of the GB structure generation and optimization given in Sec. S1 of the Supplemental Material [38]. The scheme of our calculations is shown in Fig. 2(b).

Using our code which implements the atomistic  $S$ -matrix method [22], we compute at each frequency  $\omega = n\omega_0$ , where  $n = 1, \dots, 25$  and  $\omega_0 = 10^{13}$  rad/s, the unitary  $N(\omega) \times N(\omega)$  matrix  $\mathbf{S}(\omega)$  which describes the mapping of the  $N(\omega)$  incoming bulk phonon modes to the  $N(\omega)$  outgoing bulk phonon modes on both sides of the boundary, for each GB configuration. Details of the

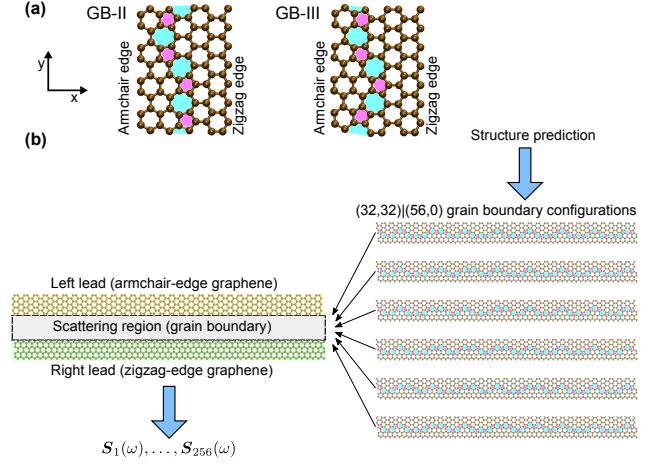


Figure 2. (a) Atomistic structure of the (4,4)|(7,0) GB-II and GB-III interfaces. (b) Schematic of atomistic  $S$ -matrix calculation with the scattering region comprising the (32,32)|(56,0) grain boundary (GB). We generate an ensemble of 256 GB configurations derived from structure predictions. Each GB configuration is inserted into the scattering region between the left and right leads and its corresponding  $S$  matrix is computed using Ref. [22].

$S$ -matrix calculations are given in Sec. S2 of the Supplemental Material [38]. In the general scattering picture [22, 37],  $\mathbf{S}(\omega)$ , which relates the incoming phonon state  $\Phi_{\text{in}}$  to the outgoing phonon state  $\Psi_{\text{out}}$  via the relation  $\Psi_{\text{out}} = \mathbf{S}(\omega)\Phi_{\text{in}}$ , encodes the amplitude and phase changes. Numerically,  $\Phi_{\text{in}}$  and  $\Psi_{\text{out}}$ , which represent a superposition of  $N(\omega)$  bulk phonon modes, are column vectors with the  $m$ -th element of  $\Phi_{\text{in}}$  ( $\Psi_{\text{out}}$ ) equal to the complex flux amplitude of the  $m$ -th incoming (outgoing) phonon channel and represented by  $[\Phi_{\text{in}}]_m = \Phi(\mathbf{k}_m)$  and  $[\Psi_{\text{out}}]_m = \Psi(\mathbf{k}_m)$  for  $m = 1, \dots, N(\omega)$  with the momentum  $\mathbf{k}_m$  and branch  $\nu_m$  associated with the  $m$ -th phonon channel. We can thus interpret  $|\Phi(\mathbf{k}')|^2$  and  $|\Psi(\mathbf{k})|^2$  as the intensity of the incoming  $\mathbf{k}'$  and the outgoing  $\mathbf{k}$  phonon flux, respectively. Hence, the matrix element  $[\mathbf{S}(\omega)]_{mn} = S(\mathbf{k}_m, \mathbf{k}'_n)$  is equal to the scattering amplitude from the  $n$ -th incoming to the  $m$ -th outgoing phonon channel, i.e.,

$$\begin{pmatrix} \Psi(\mathbf{k}_1) \\ \vdots \\ \Psi(\mathbf{k}_N) \end{pmatrix} = \begin{pmatrix} S(\mathbf{k}_1, \mathbf{k}'_1) & \dots & S(\mathbf{k}_1, \mathbf{k}'_N) \\ \vdots & \ddots & \vdots \\ S(\mathbf{k}_N, \mathbf{k}'_1) & \dots & S(\mathbf{k}_N, \mathbf{k}'_N) \end{pmatrix} \begin{pmatrix} \Phi(\mathbf{k}'_1) \\ \vdots \\ \Phi(\mathbf{k}'_N) \end{pmatrix} \quad (1)$$

where  $\{\mathbf{k}_1, \dots, \mathbf{k}_{N(\omega)}\}$  and  $\{\mathbf{k}'_1, \dots, \mathbf{k}'_{N(\omega)}\}$  denote the momenta of the outgoing and incoming modes, respectively.

The evaluation of Eq. (3) requires a configurational ensemble of  $S$  matrices computed using the method described in Ref [22], with each matrix describing a boundary configuration. For simplicity, we choose the (32,32)|(56,0) graphene GB as our boundary model which

we construct from the two lowest-energy (4,4)|(7,0) GB configurations (GB-II and GB-III in Fig. 2(a)) in Ref. [32] found using the *ab initio* random structure searching method [39]. Each (32,32)|(56,0) GB configuration comprises eight (4,4)|(7,0) GB's, a permutation of GB-II's and GB-III's, forming a continuous line of pentagon-heptagon defect pairs. This construction method yields  $2^8 = 256$  unique GB configurations. We set the direction of the phonon flux and the GB to be parallel to the  $x$ - and  $y$ -axis, respectively and impose periodic boundary conditions in the  $y$ -direction. Given the large size of the GB models, we use the empirical Tersoff potential [35], with parameters from Ref. [36], to model the C-C interatomic forces instead of more expensive *ab initio* methods. The program GULP [34] is used to optimize each GB configuration and to generate its force-constant matrices  $\mathbf{H}_{\text{CL}}$ ,  $\mathbf{H}_{\text{C}}$  and  $\mathbf{H}_{\text{CR}}$  needed for the  $S$ -matrix calculations. We also compute the force-constant matrices  $\mathbf{H}_{\text{L}}^{00}$  and  $\mathbf{H}_{\text{L}}^{01}$  ( $\mathbf{H}_{\text{R}}^{00}$  and  $\mathbf{H}_{\text{R}}^{01}$ ) describing the armchair-edge (zigzag-edge) graphene in the left (right) lead. At each frequency  $\omega = n\omega_0$  ( $n = 1, \dots, 25$  and  $\omega_0 = 10^{13}$  rad/s), we compute an  $N(\omega) \times N(\omega)$  matrix  $\mathbf{S}_\alpha(\omega)$  for the  $\alpha$ -th GB configuration ( $\alpha = 1, \dots, 256$ ).

### B. $S$ -matrix theory of boundary roughness scattering

For a nonideal boundary that consists of a deterministic part corresponding to the smooth boundary and a stochastic part describing the boundary roughness,  $\Psi_{\text{out}}$  can be partitioned into its deterministic and stochastic components in a manner akin to the treatment of randomly scattered wave fields [25–27], i.e.,

$$[\Psi_{\text{out}}]_m = \langle [\Psi_{\text{out}}]_m \rangle + [\delta\Psi_{\text{out}}]_m \quad (2)$$

where  $\langle [\Psi_{\text{out}}]_m \rangle$  and  $[\delta\Psi_{\text{out}}]_m$  are its deterministic and stochastic components, respectively, and  $\langle \dots \rangle$  represents the configurational average [40] assuming that every configuration is equally probable. Similarly, the deterministic and stochastic components of  $\mathbf{S}(\omega)$  are defined via the expression  $[\mathbf{S}(\omega)]_{mn} = \langle [\mathbf{S}(\omega)]_{mn} \rangle + [\delta\mathbf{S}(\omega)]_{mn}$  where  $\langle [\Psi_{\text{out}}]_m \rangle = \sum_{n=1}^N \langle [\mathbf{S}(\omega)]_{mn} \rangle [\Phi_{\text{in}}]_n$  and  $[\delta\Psi_{\text{out}}]_m = \sum_{n=1}^N [\delta\mathbf{S}(\omega)]_{mn} [\Phi_{\text{in}}]_n$ . For any given  $[\Phi_{\text{in}}]_n$ , the deterministic component  $\langle [\Psi_{\text{out}}]_m \rangle$  and hence  $\langle [\mathbf{S}(\omega)]_{mn} \rangle$  preserve the coherent amplitude and phase information from direct averaging.

It follows from Eq. (2) that  $\langle [\delta\Psi_{\text{out}}]_m \rangle = 0$ , i.e., the *amplitude* fluctuations of the outgoing phonon state average to zero, and thus  $\langle [\delta\mathbf{S}(\omega)]_{mn} \rangle = 0$ . However, the configurational average of  $|\langle [\Psi_{\text{out}}]_m \rangle|^2$ , the *probability* of the phonon being scattered to the  $m$ -th outgoing phonon channel, is  $\langle |[\Psi_{\text{out}}]_m|^2 \rangle = |\langle [\Psi_{\text{out}}]_m \rangle|^2 + \langle |[\delta\Psi_{\text{out}}]_m|^2 \rangle$ , implying that the transition *probability* fluctuations associated with boundary roughness are not necessarily

zero since  $\langle |[\Psi_{\text{out}}]_m|^2 \rangle \geq |\langle [\Psi_{\text{out}}]_m \rangle|^2$ . Hence, the configurational average of the transition probability is given by  $\langle |[\mathbf{S}(\omega)]_{mn}|^2 \rangle = |\langle [\mathbf{S}(\omega)]_{mn} \rangle|^2 + \langle |[\delta\mathbf{S}(\omega)]_{mn}|^2 \rangle$ , which we rewrite as  $[\mathbf{W}_{\text{total}}(\omega)]_{mn} = [\mathbf{W}_{\text{coh}}(\omega)]_{mn} + [\mathbf{W}_{\text{incoh}}(\omega)]_{mn}$  where  $\mathbf{W}_{\text{total}}$ ,  $\mathbf{W}_{\text{coh}}$  and  $\mathbf{W}_{\text{incoh}}$  are the total, coherent and incoherent transition probability matrices, respectively, with their matrix elements given by

$$[\mathbf{W}_{\text{total}}(\omega)]_{mn} = \langle |[\mathbf{S}(\omega)]_{mn}|^2 \rangle \quad (3a)$$

$$[\mathbf{W}_{\text{coh}}(\omega)]_{mn} = |\langle [\mathbf{S}(\omega)]_{mn} \rangle|^2 \quad (3b)$$

$$[\mathbf{W}_{\text{incoh}}(\omega)]_{mn} = \langle |[\mathbf{S}(\omega)]_{mn}|^2 \rangle - |\langle [\mathbf{S}(\omega)]_{mn} \rangle|^2. \quad (3c)$$

$[\mathbf{W}_{\text{total}}(\omega)]_{mn}$  represents the *total* transition probability between the  $n$ -th incoming and the  $m$ -th outgoing channel while  $[\mathbf{W}_{\text{coh}}(\omega)]_{mn}$  and  $[\mathbf{W}_{\text{incoh}}(\omega)]_{mn}$  correspond to its coherent and incoherent components.

### C. Definition of mode-resolved phonon coherence and specularity

To characterize the coherence and specularity of the  $n$ -th incoming phonon channel, we use the transition probabilities from Eq. (3) to define the phonon coherence  $\mathcal{C}_n$

$$\mathcal{C}_n(\omega) = \frac{\sum_{m=1}^{N(\omega)} [\mathbf{W}_{\text{coh}}(\omega)]_{mn}}{\sum_{m=1}^{N(\omega)} [\mathbf{W}_{\text{total}}(\omega)]_{mn}}, \quad (4)$$

the sum of the coherent transition probabilities, as its probability of being coherently scattered. Equation (4) satisfies  $0 < \mathcal{C}_n \leq 1$  and can be interpreted as the proportion of the incoming phonon flux redistributed to the outgoing phonon channels after coherent scattering. We recall that the specularity parameter is the probability that the incident phonon is scattered into the outgoing phonon channels associated with specular scattering by an ideal boundary. Given that the structural randomness of the rough boundary results in both coherent and incoherent scattering, we can characterize the specularity of each type of scattering independently. To estimate the specularity parameter associated with each type of out-scattering from the  $n$ -th incoming phonon channel at frequency  $\omega$ , we propose a statistical characterization of the ‘spread’ in the transition probabilities, given by

$$P_n^{\text{total}}(\omega) = \frac{\sqrt{\sum_{m=1}^{N(\omega)} |[\mathbf{W}_{\text{total}}(\omega)]_{mn}|^2}}{\sum_{m=1}^{N(\omega)} [\mathbf{W}_{\text{total}}(\omega)]_{mn}} \quad (5a)$$

$$P_n^{\text{coh}}(\omega) = \frac{\sqrt{\sum_{m=1}^{N(\omega)} |[\mathbf{W}_{\text{coh}}(\omega)]_{mn}|^2}}{\sum_{m=1}^{N(\omega)} [\mathbf{W}_{\text{coh}}(\omega)]_{mn}} \quad (5b)$$

$$P_n^{\text{incoh}}(\omega) = \frac{\sqrt{\sum_{m=1}^{N(\omega)} |[\mathbf{W}_{\text{incoh}}(\omega)]_{mn}|^2}}{\sum_{m=1}^{N(\omega)} [\mathbf{W}_{\text{incoh}}(\omega)]_{mn}} \quad (5c)$$

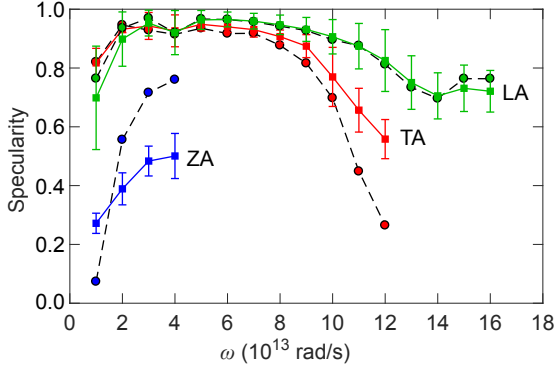


Figure 3. Comparison of the Zhao-Freund specularity parameters  $p_{\alpha,L}$  (dashed lines) from Eq. (7) with the branch-averaged specularity parameters  $\bar{P}_{\alpha,L}$  (solid lines) from Eq. (8) for  $\alpha = \text{LA}$  (green symbols),  $\text{TA}$  (red symbols) and  $\text{ZA}$  (blue symbols) phonons in armchair-edge graphene.

where  $P_n^{\text{coh}}$ ,  $P_n^{\text{incoh}}$  and  $P_n^{\text{total}}$  represent the coherent, incoherent and total specularity, respectively. Equation (5) corresponds to the normalized second moment of the transition probabilities, satisfying  $0 < P_n^{\text{total}}, P_n^{\text{coh}}, P_n^{\text{incoh}} \leq 1$ , and is related to the inverse participation ratio used to characterize disordered eigenstates in Anderson localization theory [41]. The numerator in Eq. (5) counts the effective number of outgoing channels over which the scattered energy is distributed and measures how evenly it is spread across the outgoing (transmitted and reflected) channels in different branches. The specularity parameters are related to the coherence from Eq. (4) through the compact expression

$$(P_n^{\text{total}})^2 = C_n^2 (P_n^{\text{coh}})^2 + (1 - C_n)^2 (P_n^{\text{incoh}})^2. \quad (6)$$

We motivate Eq. (5) from the advantages and consistency of its asymptotic ( $N \rightarrow \infty$ ) behavior with expected  $\mathcal{P}$  values under well-defined conditions [9]. In the Casimir ( $\mathcal{P} = 0$ ) limit where the incoming phonon energy is diffused uniformly over all  $N$  outgoing phonon channels, we have  $P_n^{\text{total}} = N^{-1/2}$  so that  $\lim_{N \rightarrow \infty} P_n^{\text{total}} = 0$ . For perfectly specular reflection ( $\mathcal{P} = 1$ ), there is only one outgoing phonon channel with a transition probability of unity (i.e.  $[\mathbf{W}_{\text{total}}(\omega)]_{mn} = 1$  for some  $m$ ) and  $P_n^{\text{total}} = 1$  as expected. For partially specular scattering ( $\mathcal{P} = p$ ) where there is one dominant outgoing phonon channel with transition probability  $p$  and the transition probability to each remaining channel is  $\frac{1-p}{N-1}$ , we obtain  $\lim_{N \rightarrow \infty} P_n^{\text{total}} = p$ .

## II. RESULTS AND DISCUSSION

### A. Comparison with Zhao-Freund specularity parameter

In addition to its consistency under well-defined conditions, we also validate Eq. (5) by comparing its predictions to the lattice dynamics-based approach from Ref. [33] in which Zhao and Freund define a frequency-dependent specularity parameter  $p(\omega)$ , which lacks modal resolution and we may consider as the specularity parameter averaged over all the modes in all phonon branches at the frequency  $\omega$ , based on the relative value of the actual phonon transmission to the transmission functions predicted from the acoustic mismatch model (AMM) and diffuse mismatch model (DMM). As we can resolve the phonon branch, we generalize the Zhao-Freund estimate to define the more precise frequency- and branch-dependent specularity parameter [33] for the left-lead  $\alpha$ -branch phonons as

$$p_{\alpha,L}(\omega) = \frac{\Xi_{\alpha,L}(\omega) - \Xi_{\alpha,L}^{(\text{DMM})}(\omega)}{\Xi_{\alpha,L}^{(\text{AMM})}(\omega) - \Xi_{\alpha,L}^{(\text{DMM})}(\omega)} \quad (7)$$

where  $\alpha = \text{LA}$  (longitudinal acoustic),  $\text{TA}$  (transverse acoustic),  $\text{ZA}$  (flexural acoustic),  $\text{LO}$  (longitudinal optical),  $\text{TO}$  (transverse optical) or  $\text{ZO}$  (flexural optical), and  $\Xi_{\alpha,L}$ ,  $\Xi_{\alpha,L}^{(\text{AMM})}$  and  $\Xi_{\alpha,L}^{(\text{DMM})}$  are the transmission functions calculated with the atomistic  $S$ -matrix, AMM and DMM method, respectively, as described in Sec. S3 of the Supplemental Material [38]. We also define the analogous branch-averaged, frequency-dependent total specularity parameter

$$\bar{P}_{\alpha,L}(\omega) = \frac{\sum_{n=1}^{N(\omega)} P_n^{\text{total}}(\omega) \Theta(v'_{x,n}) \delta_{\nu'_n, \alpha}}{\sum_{n=1}^{N(\omega)} \Theta(v'_{x,n}) \delta_{\nu'_n, \alpha}}, \quad (8)$$

by averaging  $P_n^{\text{total}}$  from Eq. (5) over all the incoming left-lead  $\alpha$ -branch phonon channels. The comparison between Eqs. (7) and (8) is made over the frequency range in which we have long-wavelength phonons with momentum  $\mathbf{k}$  satisfying  $|\mathbf{k}| < k_{\text{cutoff}}$  where the cutoff momentum  $k_{\text{cutoff}}$  is set as half of the distance between the  $\Gamma$  and  $K$ -point in the first Brillouin zone (BZ).

We observe excellent agreement between  $\bar{P}_{\text{LA},L}$  and  $p_{\text{LA},L}$  over the entire frequency range in Fig. 3. The agreement between  $\bar{P}_{\text{TA},L}$  and  $p_{\text{TA},L}$  is also remarkably good although the two quantities diverge at higher frequencies, possibly because of the deviation of the TA phonon frequencies from the linear dispersion implicitly assumed in  $\Xi_{\alpha,L}^{(\text{AMM})}$  in Eq. (7) for estimating  $p_{\text{TA},L}$ . The sensitivity of the agreement between Eqs. (7) and (8) to the phonon dispersion linearity is also reflected in the poor agreement between  $\bar{P}_{\text{ZA},L}$  and  $p_{\text{ZA},L}$  for ZA phonons, which have a *quadratic* phonon dispersion in

the long-wavelength limit in graphene [42], although the general trend of the ZA phonon specularity increasing with frequency is captured. The close agreement between Eqs. (7) and (8) for long-wavelength LA and TA phonons supports our approach for estimating the specularity parameters in Eq. (5).

## B. Specularity and coherence of graphene phonons

In Fig. 4, we analyze the reciprocal-space distribution of the phonon coherence ( $C_n$ ) and the total, coherent and incoherent specularity parameters ( $P_n^{\text{total}}$ ,  $P_n^{\text{coh}}$  and  $P_n^{\text{incoh}}$ ) for the ZA, TA and LA phonon modes over the entire first BZ in armchair-edge graphene, computed from Eqs. (5) and (4) over the frequency range of  $\omega = \omega_0$  to  $25\omega_0$  rad/s in intervals of  $\omega_0 = 10^{13}$  rad/s, using the method described in Ref. [22]. The mode-resolved data over the *entire* BZ is obtained by plotting the mode-resolved data at each frequency and then sweeping over the aforementioned frequency range. The corresponding results for zigzag-edge graphene are omitted here but given in Sec. S4 of the Supplemental Material [38]. The convergence of  $C_n$  and  $P_n^{\text{total}}$  with respect to GB width is also discussed in Sec. S5 of the Supplemental Material [38].

In Fig. 4(d), we observe that  $C_n$  for ZA phonons increases as  $k_n$  decreases, suggesting that long-wavelength ZA phonons are more sensitive to GB roughness, against conventional expectations that boundary roughness scatters short-wavelength phonons more strongly [9]. In contrast, Figs. 4(e) and (f) show that  $C_n$  for LA and TA phonons decreases as  $k_n$  increases, indicating that long-wavelength LA and TA phonons are less incoherently scattered. The trend in Fig. 4(d) is consistent with the  $P_n^{\text{total}}$  distribution in Figs. 4(g) to (i), which show  $P_n^{\text{total}}$  decreasing for LA and TA phonons but increasing for ZA phonons as  $k_n$  increases. We speculate that this is related to the significantly higher point-defect scattering rates of ZA phonons in graphene [43]. The greater GB scattering of ZA phonons implies that in suspended polycrystalline graphene, the in-plane LA and TA phonons play a more significant role in heat conduction than the out-of-plane ZA phonons which are said to dominate thermal transport in pristine graphene [42]. It has also been proposed by Soffer [14, 44] that the specularity parameter should vary *anisotropically* as  $P = \exp[-(2\eta k_x)^2]$ , where  $\eta$  is the root-mean-square surface roughness, and has no  $k_y$ -dependence. However, we do not observe such anisotropy for  $P_n^{\text{total}}$  in Figs. 4(g) to (i), indicating a disagreement with Soffer's formula. Furthermore, in the long-wavelength limit, the  $P_n^{\text{total}}$  for ZA phonons does not converge to unity as suggested by the formula.

## C. Coherent vs. incoherent specularity parameters

It is widely assumed [19, 23, 24] that coherent (incoherent) scattering is perfectly specular (diffuse), i.e.,  $P_n^{\text{coh}} = 1$  ( $P_n^{\text{incoh}} = 0$ ), although there is no direct evidence for this relationship. Underlying this assumption is the idea that the perfect interface is smooth although at the atomistic level, lattice imperfections must occur because of the crystallographic discontinuity. Given this assumption, it follows from Eq. (6) that coherence is equivalent to specularity ( $C_n = P_n^{\text{total}}$ ). We exploit our ability to distinguish coherent from incoherent scattering to analyze how specularity actually depends on coherence, by comparing the  $P_n^{\text{coh}}$  and  $P_n^{\text{incoh}}$  distributions in Figs. 4(j) to (o). The corresponding  $P_n^{\text{coh}}$  and  $P_n^{\text{total}}$  distributions generally have similar  $k_n$ -dependence, with  $P_n^{\text{coh}} > P_n^{\text{total}}$  because incoherent scattering is strongly diffuse ( $P_n^{\text{incoh}} \ll 1$ ) with no significant  $k_n$ -dependence for ZA, TA and LA phonons, as can be seen in Figs. 4(m) to (o), and Eq. (6) implies that  $P_n^{\text{total}} < \max\{P_n^{\text{coh}}, P_n^{\text{incoh}}\}$ . The near uniform small value of  $P_n^{\text{incoh}}$  over the entire BZ in Figs. 4(m) to (o) also suggests that the diffuse character of incoherent scattering is captured by Eq. (5c).

Like in Fig. 4(g), the  $P_n^{\text{coh}}$  distribution for ZA phonons in Fig. 4(j) is significantly smaller than unity, indicating that even coherent scattering is not fully specular for out-of-plane polarized phonons. The  $P_n^{\text{coh}}$  distribution for LA and TA phonons in Fig. 4(k) and (l) show that the coherent specularity diverges from unity as we move away from the BZ center. To explain the reduced ZA phonon specularity ( $P_n^{\text{total}}$ ), we compare the main scattering transitions for an incoming armchair-edge graphene (a) ZA and (b) TA phonon at normal incidence ( $k_y = 0$ ) to the boundary at a single frequency of  $\omega = 5\omega_0$  rad/s in Fig. 5. The incoming ZA phonon is forward-scattered to several outgoing channels while the incoming TA phonon is forward-scattered to a single outgoing channel on the zigzag-edge side. The distinctive periodic arrangement in the distribution of the main outgoing ZA phonon channels, separated by an interval of  $\Delta k_y$ , is due to diffraction by the smooth part of the boundary which has a periodicity equal to  $W_{\text{GB}}$  the width of the constituent (4,4)|(7,0) GB such that  $\Delta k_y = 2\pi/W_{\text{GB}}$ . For a clear representation of diffraction by the 'smooth' boundary with the aforementioned transverse periodicity, we plot the equivalent scattering transitions for the pure GB-II and GB-III boundaries in Sec. S6 of the Supplemental Material [38]. A similar effect has also been reported for molecular dynamics simulations of symmetric graphene GB's [45]. This diffractive scattering is seen for other ZA phonon channels but none of the in-plane LA and TA phonons.

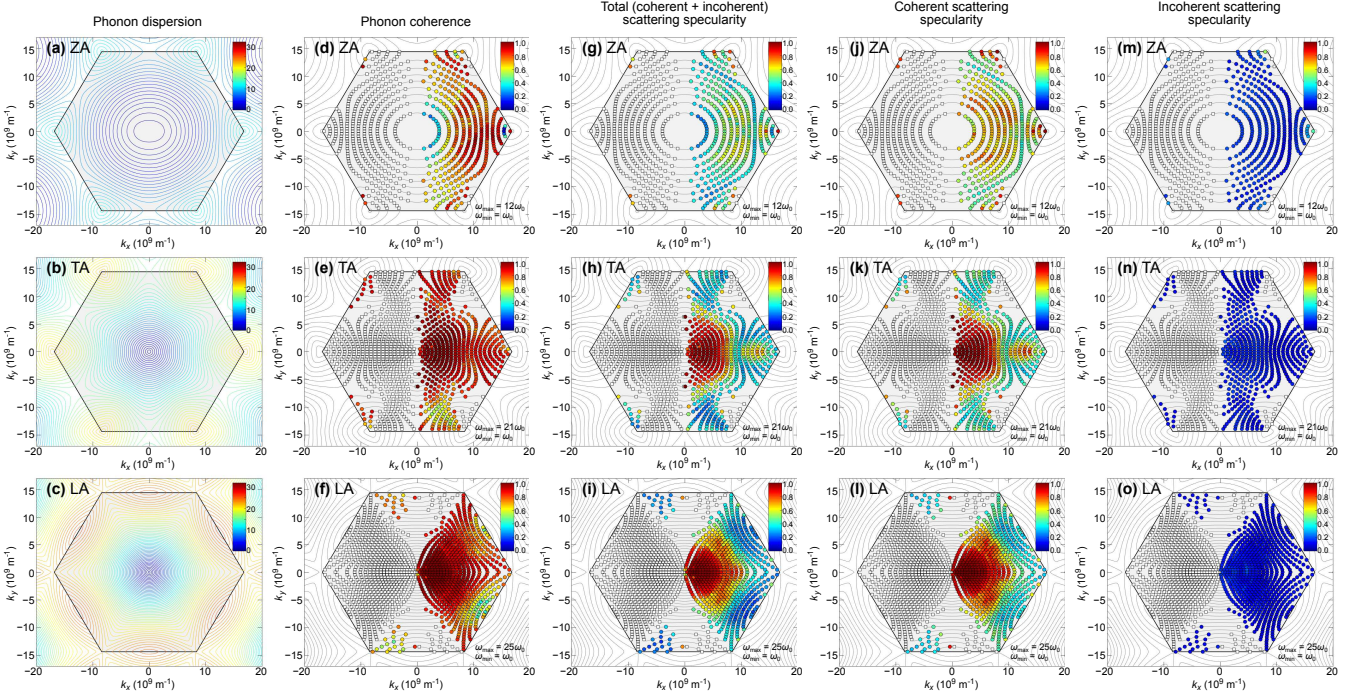


Figure 4. **(a-c)** Phonon dispersion, **(d-f)** coherence ( $C_n$ ) and the estimated **(g-i)** total, **(j-l)** coherent and **(m-o)** incoherent mode-resolved specularity parameters ( $P_n^{\text{total}}$ ,  $P_n^{\text{coh}}$  and  $P_n^{\text{incoh}}$ ) for the ZA, TA and LA phonons in armchair-edge graphene impinging on the grain boundary. The modes in the incoming phonon flux are filled circles colored according to their numerical value while the modes in the outgoing flux are hollow squares. The frequency range is  $\omega = \omega_0$  to  $25\omega_0$  where  $\omega_0 = 10^{13}$  rad/s, with the maximum frequency ( $\omega_{\text{max}}$ ) for the ZA, TA and LA phonons equal  $12\omega_0$ ,  $21\omega_0$  and  $25\omega_0$ , respectively. The isofrequency contours are indicated in intervals of  $\Delta\omega = \omega_0$  in **(d-o)** using solid gray lines. The phonon dispersions in **(a-c)** are indicated with color contours in intervals of  $\Delta\omega = \omega_0/2$ .

### III. SUMMARY

We have formulated an  $S$  matrix-based theory of boundary roughness scattering to predict the mode-resolved coherence and specularity parameters and applied it to the (32,32)|(56,0) graphene GB. The predicted specularity parameters are shown to be consistent with those of Zhao and Freund [33]. We find that phonon scattering is predominantly coherent for graphene GB's although contrary to expectations, coherence and specularity are lowest for long-wavelength ZA phonons because of diffractive scattering by the GB, while the opposite trend is seen for LA and TA phonons. Our results also demonstrate that incoherent scattering is much more diffuse than coherent scattering and that coherence and specularity are not necessarily equivalent. Given its generality, our method can be applied in a straightforward manner to analyze phonon coherence and specularity in other atomistic boundary models.

ZYO acknowledges financial support from a grant from the Science and Engineering Research Council (Grant No. 152-70-00017) and the Agency for Science, Technology, and Research (A\*STAR), Singapore. GS acknowledges support from EPSRC grant No.EP/J010863/2 and

a grant from Tohoku University. CJP is supported by the Royal Society through a Royal Society Wolfson Research Merit award.

---

\* ongzy@ihpc.a-star.edu.sg

- [1] A. I. Hochbaum, R. Chen, R. D. Delgado, W. Liang, E. C. Garnett, M. Najarian, A. Majumdar, and P. Yang, *Nature* **451**, 163 (2008).
- [2] J. Lim, K. Hippalgaonkar, S. C. Andrews, A. Majumdar, and P. Yang, *Nano Lett.* **12**, 2475 (2012).
- [3] D. Li and A. J. H. McGaughey, *Nanoscale Microsc. Thermophys. Eng.* **19**, 166 (2015).
- [4] C. Monachon, L. Weber, and C. Dames, *Annual Review of Materials Research* **46**, 433 (2016).
- [5] R. A. Guyer and J. A. Krumhansl, *Phys. Rev.* **148**, 766 (1966).
- [6] Z. Ding, J. Zhou, B. Song, V. Chiloyan, M. Li, T.-H. Liu, and G. Chen, *Nano Lett.* **18**, 638 (2018).
- [7] M.-H. Bae, Z. Li, Z. Aksamija, P. N. Martin, F. Xiong, Z.-Y. Ong, I. Knezevic, and E. Pop, *Nature Communications* **4**, 1734 (2013).
- [8] G. Chen, *J. Heat Transfer* **119**, 220 (1997).
- [9] G. Chen, *Nanoscale energy transport and conversion: a parallel treatment of electrons, molecules, phonons, and photons* (Oxford University Press, New York, 2005).

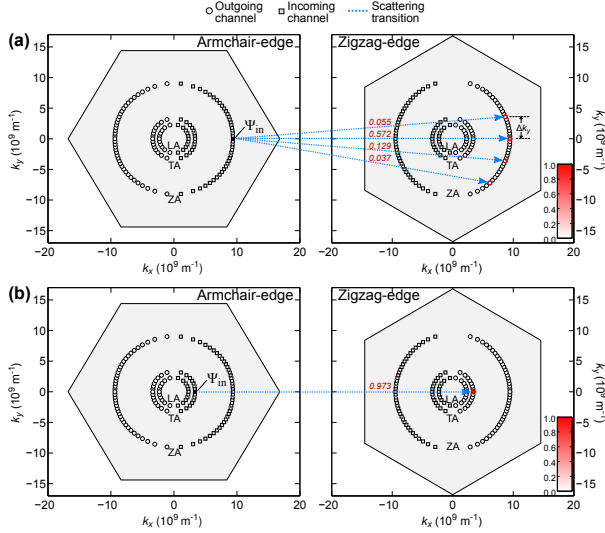


Figure 5. Main scattering transitions for an incoming (a) ZA and (b) TA phonon, labeled  $\Psi_{in}$ , at normal incidence to the grain boundary from the armchair-edge graphene on the left at  $\omega = 5 \times 10^{13}$  rad/s. The bulk LA, TA and ZA phonon channels on the armchair-edge (left subpanel) and zigzag-edge (right subpanel) graphene side are displayed within their respective first Brillouin zones. The color scales indicate the transition probability from  $\mathbf{W}_{total}(\omega)$  for the dominant outgoing channels, with the transitions indicated by dotted lines and transition probabilities written in *italic font*.

- [10] N. K. Ravichandran, H. Zhang, and A. J. Minnich, *Phys. Rev. X* **8**, 41004 (2018).
- [11] P. K. Schelling, S. R. Phillpot, and P. Keblinski, *Applied Physics Letters* **80**, 2484 (2002).
- [12] P. K. Schelling, S. R. Phillpot, and P. Keblinski, *J. Appl. Phys.* **95**, 6082 (2004).
- [13] L. N. Maurer, S. Mei, and I. Knezevic, *Phys. Rev. B* **94**, 45312 (2016).
- [14] C. Shao, Q. Rong, M. Hu, and H. Bao, *J. Appl. Phys.* **122**, 155104 (2017).
- [15] C. Shao, Q. Rong, N. Li, and H. Bao, *Phys. Rev. B* **98**, 155418 (2018).
- [16] Z. Aksamija and I. Knezevic, *Phys. Rev. B* **82**, 45319 (2010).
- [17] A. K. Majee and Z. Aksamija, *Phys. Rev. B* **93**, 235423 (2016).
- [18] B. Yang and G. Chen, *Phys. Rev. B* **67**, 195311 (2003).
- [19] M. N. Luckyanova, J. Garg, K. Esfarjani, A. Jandl, M. T. Bulsara, A. J. Schmidt, A. J. Minnich, S. Chen, M. S. Dresselhaus, Z. Ren, and Others, *Science* **338**, 936 (2012).
- [20] J. Ravichandran, A. K. Yadav, R. Cheaito, P. B. Rossen, A. Soukiassian, S. J. Suresha, J. C. Duda, B. M. Foley, C.-H. Lee, Y. Zhu, and Others, *Nature Materials* **13**, 168 (2014).
- [21] Y. Wang, H. Huang, and X. Ruan, *Phys. Rev. B* **90**, 165406 (2014).
- [22] Z.-Y. Ong, *Phys. Rev. B* **98**, 195301 (2018).
- [23] A. A. Maznev, *Phys. Rev. B* **91**, 134306 (2015).
- [24] F. Shi, M. Lowe, and R. Craster, *Phys. Rev. B* **95**, 214305 (2017).
- [25] M. Lax, *Rev. Mod. Phys.* **23**, 287 (1951).
- [26] A. Ishimaru, in *Wave Propagation and Scattering in Random Media*, edited by A. Ishimaru (Academic Press, New York, New York, 1978) pp. 69–92.
- [27] J. A. Ogilvy, *Reports on Progress in Physics* **50**, 1553 (1987).
- [28] L. L. Foldy, *Phys. Rev.* **67**, 107 (1945).
- [29] V. Twersky, *J. Acoust. Soc. Am.* **29**, 209 (1957).
- [30] V. Twersky, *J. Math. Phys.* **3**, 700 (1962).
- [31] D. Kechrakos, *J. Phys.: Condens. Matter* **2**, 2637 (1990).
- [32] G. Schusteritsch and C. J. Pickard, *Phys. Rev. B* **90**, 35424 (2014).
- [33] H. Zhao and J. B. Freund, *J. Appl. Phys.* **105**, 13515 (2009).
- [34] J. D. Gale and A. L. Rohl, *Mol. Simul.* **29**, 291 (2003).
- [35] J. Tersoff, *Phys. Rev. Lett.* **61**, 2879 (1988).
- [36] L. Lindsay and D. A. Broido, *Phys. Rev. B* **81**, 205441 (2010).
- [37] Z.-Y. Ong, *J. Appl. Phys.* **124**, 151101 (2018).
- [38] See Supplemental Material at [URL will be inserted by publisher] for details on the generation and optimization of the (32,32)|(56,0) grain boundary configurations, the *S*-matrix calculation methodology, the definition of the branch-resolved transmission functions, the simulation results for zigzag-edge graphene, the convergence of simulation results for phonon coherence, total specularity and transmission, and ZA and TA phonon scattering at pure GB-II and GB-III interface.
- [39] C. J. Pickard and R. J. Needs, *Phys. Rev. Lett.* **97**, 45504 (2006).
- [40] P. C. Waterman and R. Truell, *J. Math. Phys.* **2**, 512 (1961).
- [41] J. T. Edwards and D. J. Thouless, *J. Phys. C* **5**, 807 (1972).
- [42] L. Lindsay, D. A. Broido, and N. Mingo, *Phys. Rev. B* **82**, 115427 (2010).
- [43] C. A. Polanco and L. Lindsay, *Phys. Rev. B* **97**, 14303 (2018).
- [44] S. B. Soffer, *J. Appl. Phys.* **38**, 1710 (1967).
- [45] E. E. Helgee and A. Isacsson, *Phys. Rev. B* **91**, 205432 (2015).